The Relation Between Precursor Gas Flows,Thickness Dependent Material Phases, andOpto-Electrical Properties of Dopeda/nc-SiOX≥0:H Films

de Vrijer, Thierry; Smets, Arno H.M.

DOI
10.1109/JPHOTOV.2021.3059940

Publication date
2021

Document Version
Final published version

Published in
IEEE Journal of Photovoltaics

The Relation Between Precursor Gas Flows, Thickness Dependent Material Phases, and Opto-Electrical Properties of Doped a/nc-$SiO_{X\geq 0}$:H Films

Thierry de Vrijer and Arno H.M. Smets

***Abstract*—Doped layers are a determining factor for the performance of photovoltaic devices such as silicon heterojunction and thin film silicon solar cells. The material properties of doped hydrogenated amorphous/nanocrystalline silicon-oxide (a/nc-$SiO_{X\geq 0}$:H) films processed by plasma-enhanced chemical vapor deposition generally exhibit a tradeoff between optical and electrical performance. The optoelectrical properties are the result of different material phases in these heterogeneous films, such as hydrogenated amorphous silicon and silicon-oxide tissue, nanocrystalline silicon grains, their corresponding fractions and extent of doping. In this article, all the precursor gas flows are varied to achieve a wide range of doped a/nc-$SiO_{X\geq 0}$:H phases. A material phase diagram is introduced to clarify the complex interplay between processing conditions, dominant growth mechanisms, a/nc-$SiO_{X\geq 0}$:H phases, and the resulting optoelectrical properties. In addition, it is discussed that material properties are strongly dependent on the thickness of the films, as the mix of different material phases is not uniform along the growth direction.**

***Index Terms*—Doped silicon, material growth, material phases, nanocrystalline silicon, PECVD, precursor gas, silicon oxide.**

I. Introduction

THE efficiency of photovoltaic devices in which thin film silicon layers are integrated is strongly influenced by the properties of the doped layers. Such devices include silicon heterojunction solar cells [1]–[3], hybrid amorphous silicon/CIGS tandem devices [4], micromorph solar cells [5]–[7] and hybrid perovskite/c-Si tandem devices [8]. The doped silicon layers have a variety of multifunctional applications in these devices. Generally, the functionalities require optically transparent doped layers with high transverse conductivity. There exists a tradeoff however between the optical and electrical properties of the layers [9]–[11]. Which particular property should be prioritized, such as a high optical bandgap for a window layer, the refractive index for an intermediate reflective layer, or the transverse conductivity in a tunnel recombination junction, depends on the particular application.

It was previously demonstrated that the optoelectrical tradeoff in doped silicon films results from an interplay between the development of a crystalline phase and oxygen integration in the amorphous phase [12], [13], as well as the density of the amorphous phase [14], [15]. An in-depth understanding of the material growth of the doped layers is, therefore, crucial for the production of an optimal device.

In this article, we have investigated the influence of the precursor gas flow rates and thickness on the properties of p- and n-doped hydrogenated amorphous and nanocrystalline silicon and silicon-oxide (a/nc-$SiO_{X\geq 0}$:H) films.

II. Experimental Details

The doped films are deposited on Corning Eagle XG glass, cut in 10 × 2.5 cm strips. For processing, a radiofrequency (RF) plasma enhanced chemical vapor deposition (PECVD) cluster tool, operating at a frequency of 13.56 MHz is used. In this cluster tool p-doped films and n-doped films are processed in separate dedicated chambers. Recipes were developed earlier for the doped hydrogenated silicon oxide (SiO_X:H) layers such that the films provide adequate initial performance in terms of both their optical and electrical performance for window layer applications in thin film solar cells [14], [16]. Based on this, in this article, the material properties of the doped films are further characterized within a relatively small optimal range. The deposition parameters of the doped silicon layers and the ranges used for the precursor gas flow rates are given in Table I. The reported films have a thickness of ∼60–80 nm, unless specifically mentioned otherwise. The deposition rates given in Table I are the result of the full set of deposition conditions and indicates the range of deposition rates for all p-doped and n–doped films presented in this article. The diborane (B_2H_6) and phosphine (PH_3) precursors are diluted in H_2, such that the reported B_2H_6 gas flow rate consists of 0.02% diborane and the PH_3 flow rate consist of 2% phosphine.

Manuscript received August 25, 2020; revised November 15, 2020 and January 8, 2021; accepted February 11, 2021. Date of publication March 8, 2021; date of current version April 21, 2021. This work was supported by the Netherlands Organization for Scientific Research (NWO) Solar to Products Grant awarded to Arno Smets and the support provided by Shell International Exploration & Production New Energies Research & Technology Dense Energy Carriers Program. *(Corresponding author: Thierry de Vrijer.)*

The authors are with the Photovoltaic Materials and Devices Group (PVMD), ESE, Delft University of Technology, 2628 Delft, The Netherlands (e-mail: t.devrijer@tudelft.nl; a.h.m.smets@tudelft.nl).

Color versions of one or more figures in this article are available at https://doi.org/10.1109/JPHOTOV.2021.3059940.

Digital Object Identifier 10.1109/JPHOTOV.2021.3059940

TABLE I
DEPOSITION PARAMETERS OF THE DOPED FILMS. FOR THE GAS FLOW RATES THE RANGE INVESTIGATED IN HIS WORK IS INDICATED. THE DEPOSITION RATES ARE A RESULT OF THE DEPOSITION CONDITIONS AND INDICATE THE HIGHEST AND LOWEST DEPOSITION RATE FOR THE P-DOPED AND N-DOPED SAMPLES PRESENTED IN THIS ARTICLE, RESPECTIVELY

H_2 (sccm)	170-200	100-120
CO_2 (sccm)	0-2.3	0-2.4
B_2H_6 (200ppm in H_2) (sccm)	10-40	-
PH_3 (2% in H_2) (sccm)	-	1.2-3.6
Pressure (mbar)	2.2	1.5
Substrate Temperature (°C)	180	180
Power density (mW/cm^2)	90.3	69.4
Depostion rate (nm/s)	0.015-0.047	0.011-0.019

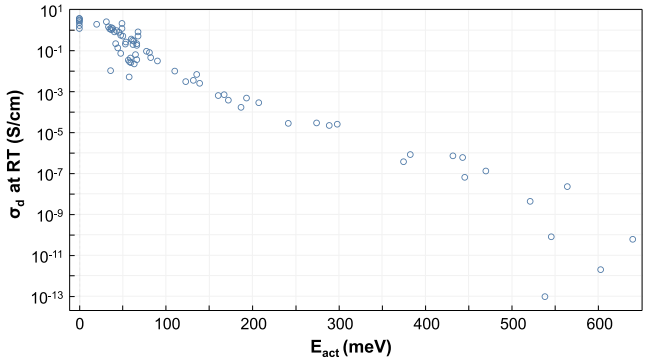

Fig. 1. Dark conductivity (σ_d) at room temperature plotted as a function of activation Energy ($E_{\rm act}$) on a semilogarithmic plot, for all processed samples.

Incorporation of oxygen happens during processing through addition of a CO_2 precursor gas, and it not a postdeposition oxidation process. Energy-dispersive X-ray spectroscopy measurements of a few p-doped SiO_X:H (p-SiOx:H) samples indicated an atomic fraction of carbon in the films of below 1%, as a result of the CO_2 precursor. It is, therefore, assumed that carbon integration does not play a significant role in the presented results.

To perform dark conductivity measurements, parallel electrodes consisting of 500-nm-thick aluminium bars were deposited onto the films using electron beam evaporation. These measurements were performed by measuring the current conducted between two electrodes at a fixed voltage of 10V and temperature in a dark environment. By repeating this measurement at 5 °C intervals, from 130 °C to 60 °C, the activation energy ($E_{\rm act}$) and dark conductivity at room temperature can be calculated using the Arrhenius equation

$$k_{\rm B}T = -E_{\rm act}\ \ln\frac{\sigma_0}{\sigma}. \tag{2.1}$$

Here, σ is the conductivity, σ_0 is the material dependent conductivity constant, $k_{\rm B}$ is Boltzmann's constant and T is the temperature in Kelvin. The $E_{\rm act}$ and dark conductivity at room temperature (σ_d) showed very similar trends, with high σ_d's at low $E_{\rm act}$'s. This is shown in Fig. 1, where the σ_d of all measured samples is plotted as a function of the $E_{\rm act}$. The $E_{\rm act}$ is, therefore, used in this article as a metric for the electrical performance of the doped a/nc-$SiO_{X\geq 0}$:H films.

A J.A. Woollam spectroscopic ellipsometer was used to determine the refractive index and the optical bandgap (E_{04}). The spectroscopic ellipsometry (SE) measurements were fitted to an effective medium model using the Bruggeman analysis mode. a/nc-$SiO_{X\geq 0}$:H is a heterogeneous material consisting of an amorphous structure of hydrogenated amorphous silicon (a-Si:H), amorphous silicon-oxide (a-SiO_X:H) and crystalline grains. Therefore, the material properties of SiO_2 and a-Si:H are used to mimic the a-SiO_X:H and a-Si:H tissue and polycrystalline silicon is used to mimic the crystalline grains. Consequently, the model uses the material properties of SiO_2, obtained from [17], a-Si:H, obtained from in-house measurements (Cody-Lorentz oscillator: Amp = 122. Br = 2.55, E_0 = 3.59, E_g = 1.62, E_p = 1.94, E_t = 0.00, and E_u = 0.5) and polycrystalline silicon (poly-Si_g2) that is available in the material library of the CompleteEASE software offered for Woollam, to approximate the optical properties of doped a/nc-$SiO_{X\geq 0}$:H material. This is approach is similar to [18] and to [6] with a minor modification. Through this approach the silicon-oxide phase fraction ($R_{\rm SiOx}$) is obtained indirectly. In [18], the oxygen content obtained through this approach was found to be consistent with the content deduced from X-ray photoelectron spectroscopy. In this article, the observed trends in $R_{\rm SiOx}$, as a function of deposition conditions, were found to be consistent with trends observed in the peak intensity of the stretching modes related to silicon-oxide bonds obtained from Raman spectroscopy measurements.

In this article, the E_{04} optical bandgap is used to describe trends in the optical absorption of the films. The different phases in the heterogeneous a/nc-$SiO_{X\geq 0}$:H material each retain their own respective electrical bandgap energy. The E_{04} can therefore be considered an effective optical bandgap, reflecting variations in the material phase fractions and quality of the amorphous phase. This definition is often used for heterogeneous mixed phase materials [10], [14], [18]–[20], for which determining a single electrical bandgap energy is non-trivial and often arbitrary. The E_{04} was determined by calculating the photon energy level at which the absorption coefficient equals 10^4 cm^{-1}.

Additional structural analysis was performed through Raman spectroscopy, using an inVia confocal Raman microscope with a laser operating at a wavelength of 514 nm. The crystallinity of the films was obtained from these measurements by fitting a Gaussian distribution with a peak at a Raman shift of 520 cm^{-1} corresponding to the crystalline silicon phase and by fitting Gaussians at 160, 320, 390, and 480 cm^{-1} corresponding to transverse acoustic (TA), longitudinal acoustic (LA), longitudinal optic (LO), and transverse optic (TO) amorphous silicon phonon modes, respectively. The crystallinity ($\chi_{\rm C}$) in this article

is defined by

$$\chi_{\mathrm{C}} = \frac{I_{\mathrm{c-Si}}}{I_{\mathrm{c-Si}} + \gamma \cdot I_{\mathrm{a-Si}}}. \tag{2.2}$$

Here, $I_{\mathrm{c\text{-}Si}}$ is the integrated area under the Gaussian distribution at 520 cm^{-1} corresponding to the crystalline silicon phase and $I_{\mathrm{a\text{-}Si}}$ for the peak at 480 cm^{-1} corresponding to the amorphous phase. γ is a correction factor for the difference in cross section for phonon excitation of c-Si with respect to a-Si and equals 0.8, similar to [21], [22]. Consequently, the χ_{C} indicates the crystalline fraction of the silicon phase and does not take the amorphous silicon-oxide phase into account. This means that the total fraction of the doped a/nc-$\mathrm{SiO_{X\geq 0}}$:H material that is crystalline, so the crystalline phase fraction ($R_{c\text{-}\mathrm{Si}}$) is equal to

$$R_{c-\mathrm{Si}} = \chi_{\mathrm{C}} \ (1 - R_{\mathrm{SiO}x}). \tag{2.3}$$

Regarding Experimental Error: The thickness, $R_{\mathrm{SiO}x}$ and E_{04} are extracted from SE measurements. All model fits have a mean square error between 2 and 7. For these fits, the thickness has an error margin between 0.1%–0.9%, the SiO_2, a-Si:H and poly-Si material fractions have an relative error margin of 0.1%–2%. For a number of selected samples five points were measured on a single film. Based on these measurements a maximum error margin of $\pm$ 0.02eV can be reported for the E_{04}, $\pm$2.2 nm for the thickness and $\pm$0.15% absolute for the SiO_2 material fraction. Similarly, multiple Raman measurements on a single sample showed an error margin of 3.13% absolute for the crystallinity values reported in this article. A similar procedure was performed for the dark conductivity measurements, for 4 different sets of contacts on a single film. The resulting E_{act} values showed an maximum error margin of $\pm$ 7 meV.

These reported values give insight into the combined error introduced by the measurement setups, model fits and sample uniformity. As to error in reproducibility, although each sample with its unique combination of deposition conditions and deposition time was produced only once, the very large sample size of over 75 films is a testament to the reproducibility and validity of the reported trends.

III. Results and Discussion

A. Influence of Precursor Gas Flow Rates

We start with the influence of the precursor gasses on the properties of p-doped films. All precursor gas flow rates are reported relative to the silane flow rate ($F_{\mathrm{gas/SiH4}}$). Changes in the deposition parameters of the films, such as the relative precursor gas flow rates, influence the plasma conditions. The plasma conditions in turn affect the growth of the doped a/nc-$\mathrm{SiO_{X\geq 0}}$:H material. This becomes apparent through changes in properties, such as the crystallinity, the active dopant concentration, the density of the amorphous silicon phase, and the oxygenation of the amorphous phase. The material growth in turn influences the optoelectrical behavior of the doped films. Therefore, to properly understand the complex influence of the relative precursor gas flow rates, we first look at the grown material. Using the the silicon-oxide phase fraction (R_{SiOx}), obtained from SE measurements, and the crystalline phase fraction ($R_{c\text{-}\mathrm{Si}}$), obtained from Raman measurements, of the films, material phase plots are developed and presented in Fig. 2, to qualitatively visualize the effects of the relative gas flow rates on the a/nc-$\mathrm{SiO_{X\geq 0}}$:H material growth. Even though the extent of oxidation of the a-SiOx:H can vary, the a-Si and a-$\mathrm{SiO_X}$:H are shown as separate material phase fractions as these phases can coexist in the heterogenous material [12], [13]. Moreover, it supports visualization of both the level of oxidation and the transition from an a/nc-Si:H to an a/nc-SiOx:H material.

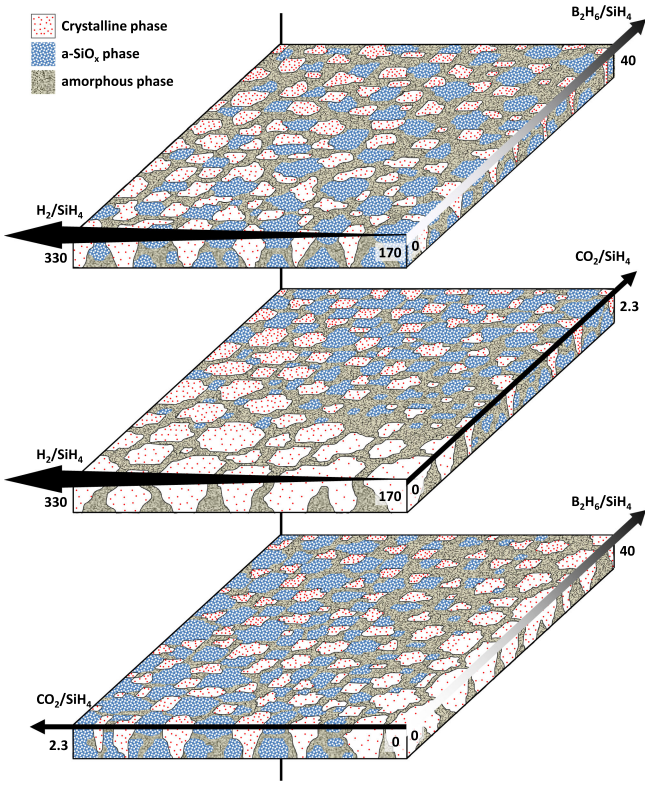

Fig. 2. Material phase diagrams of p-doped silicon materials as a function of the relative H_2 and B_2H_6 flow rates (top), CO_2 and H_2 flow rates (middle), and CO_2 and B_2H_6 flow rates (bottom). The blue/white areas indicate an amorphous silicon oxide phase. The grey areas indicate an amorphous silicon phase. The white areas with red dots indicate a crystalline silicon phase. The plain arrow with solid fill indicates direction of increasing $\mathrm{F_{CO2/SiH4}}$. The plain arrow with gradient fill indicates effect of increasing $\mathrm{F_{B2H6/SiH4}}$. The widening arrow with solid fill indicates the effect of increasing $\mathrm{F_{H2/SiH4}}$.. These conventions are similar to those in Figs. 3–5. Each plot is the result of connecting 12 parts, a 4x3 matrix. For each part the $R_{\mathrm{SiO}x}$ obtained from SE measurements was used to determine the a-SiOx phase, while the $R_{c\text{-}\mathrm{Si}}$, obtained from Raman measurements, was used to determine the c-Si phase. The red dots in the crystalline phase represent the dopants, while the density of red dots indicates the active dopant concentration. The active dopant concentration is not obtained from direct measurement, but rather indicates an educated guess of the active dopant concentration relative to the other processed samples. This estimation is based on trends in the dark conductivity measurements and $R_{c\text{-}\mathrm{Si}}$, operating under the assumption that the measured dark conductivity is a function of the $R_{c\text{-}\mathrm{Si}}$ and active dopant concentration. The potential effect crystalline grain connectivity and grain passivation are consequently not considered.

Fig. 2 shows that, as a function of the precursor gas flow rates, the a-Si:H, a-SiOx:H, and crystalline silicon phase fractions present in the material can change significantly.

The middle plot for instance shows that when $F_{\mathrm{H2/SiH4}}$ is decreased and $F_{\mathrm{CO2/SiH4}}$ is increased, the material changes

from high crystallinity nanocrystalline silicon to predominantly amorphous silicon oxide. If we look at the effect of $F_{CO2/SiH4}$ in particular, in Fig. 2 (middle, bottom), we see that an increase of $F_{CO2/SiH4}$ results in an increase of the R_{SiOx}, while crystalline growth is suppressed. For instance, when $F_{CO2/SiH4}$ is increased from 0 to 2.3 R_{SiOx} is increased from 15%–28% to 41%–52%, depending on $F_{B2H6/SiH4}$ and $F_{H2/SiH4}$. An increase of $F_{H2/SiH4}$, on the other hand, generally results in a higher crystallinity, which can also be observed in Fig. 2 (top, middle). This relation between the H_2 flow rate and crystallinity will be discussed in more detail later.

The effect of the relative dopant flow rate $F_{B2H6/SiH4}$ is rather more complex, as observed in Fig. 2 (top, bottom). For one, the dopant precursor suppresses crystalline growth [12], [23], [24]. Raman measurements show that the crystallinity continually decreases with increasing $F_{B2H6/SiH4}$. At $F_{H2/SiH4}$ of 170 for instance, depending on the relative CO_2 flow rate, the $R_{c\text{-}Si}$ of the silicon phase decreases 18%–20% when $F_{B2H6/SiH4}$ is increased from 10 to 40. Increasing the $F_{B2H6/SiH4}$ also leads to a decrease of the relative a-SiO_X:H material phase. The R_{SiOx} of the films with $F_{CO2/SiH4}\approx 1.4$ and $F_{H2/SiH4} = 170$, for instance, decreases from 46% to 17% when $F_{B2H6/SiH4}$ is increased from 10 to 40.

We have briefly discussed the effect of changes in the plasma conditions, through variations in the precursor gas flow rates, on the material phases in the doped a/nc-$SiO_{X\geq 0}$:H films. We can now consider the effect these material phase changes have on the optoelectrical properties. These effects can be observed in Fig. 3. The material growth is a result of the delicate interplay between the different precursor gas flows. For that reason a single plot has been developed for the E_{act} and for the E_{04}, to visualize a large number of data points, rather than a large number of plots with fewer data points. The various data points are the result of variations in the relative B_2H_6, H_2, and CO_2 flow rates. Variations in the B_2H_6 are indicated by the depth of color, variations in the H_2 flow rate are indicated by the icon size and open/closed symbol nature, while the relative CO_2 flow rate is plotted on the x-axis. This means that the effect of varying a single deposition parameter can be observed by considering symbols of a certain size/color at a fixed x-axis position. As a visual aid, arrows of different styles have been introduced in the figure to describe different trends. Please note that the arrow style and fill used for certain $F_{gas/SiH4}$ in Fig. 2 match those used in Figs. 3 –5.

First, an increase of $F_{CO2/SiH4}$ increases both the E_{act} (see Fig. 3 ↑1) and the E_{04} (see Fig. 3 ↑2) of the doped layers. The increase of the E_{04} is clearly visible for each combination of gas flow rates. The increase of E_{04} with increasing R_{SiOx} has been widely reported [13], [14], [19], [20], [25], [26]. The influence of $F_{CO2/SiH4}$ on the electrical properties is less pronounced, though still significant at relatively high H_2 flow rates. The p-doped hydrogenated nanocrystalline silicon (p-nc-Si:H) samples for instance, deposited without CO_2 precursor, have an E_{act} of around 35 meV, which is increased to around 60 meV at $F_{CO2/SiH4}\approx 1.7$ and between 80 and 160 meV for $F_{CO2/SiH4} = 2.33$. These trends are the result of an increase of the R_{SiOx} and decrease of the $R_{c\text{-}Si}$.

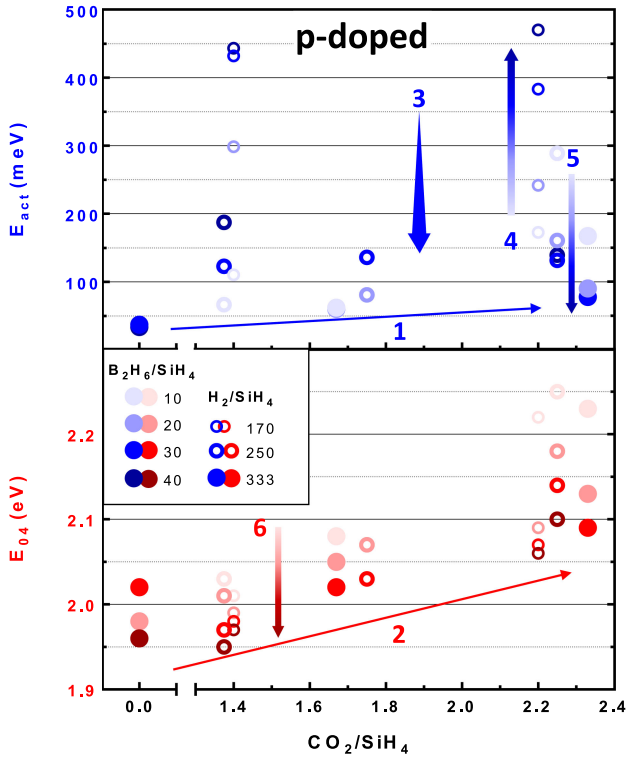

Fig. 3. E_{act} (top) and E_{04} (bottom) of p-doped a/nc-$SiO_{X\geq 0}$:H films as a function of the relative CO_2 flow rate ($F_{CO2/SiH4}$). The brightness/depth of color of the markers indicates the relative doping flow rate ($F_{B2H6/SiH4}$) while the size of the markers and their open/closed nature indicates the relative hydrogen flow rate ($F_{H2/SiH4}$). Arrows, added to indicate trends in the data, are referenced in the article. ↑1-2 indicate the influence of $F_{CO2/SiH4}$. ↑3 indicates the influence of $F_{H2/SiH4}$. ↑4–6 indicate the influence of $F_{B2H6/SiH4}$.

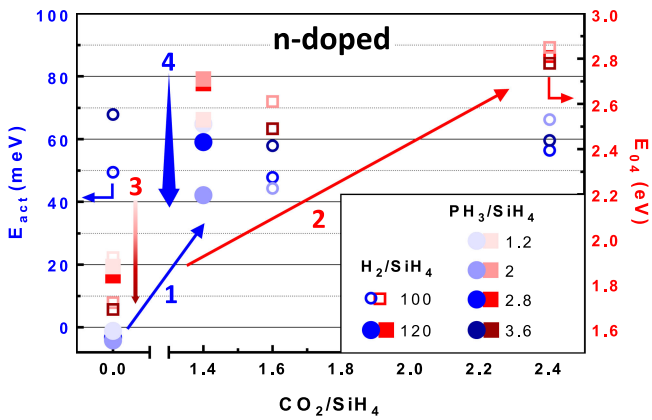

Fig. 4. E_{act} (left, circles) and E_{04} (right, squares) n-doped a/nc-$SiO_{X\geq 0}$:H films as a function of $F_{CO2/SiH4}$. The brightness/depth of color of the markers indicates the $F_{PH3/SiH4}$ while the size of the markers and their open/closed nature indicates $F_{H2/SiH4}$. Arrows, added to indicate trends in the data, are referenced in the article. ↑1-2 indicate the influence of $F_{CO2/SiH4}$. ↑3 indicates the influence of $F_{PH3/SiH4}$. ↑4 indicates the influence of $F_{H2/SiH4}$.

An increase of the hydrogen flow rate generally results in a lower E_{act} (see Fig. 3 ↑3), which is a consequence of the increasing $R_{c\text{-}Si}$. A higher $R_{c\text{-}Si}$ likely indicates an improvement of the macroscopic conductive properties of the film as a result of more or larger crystalline grains with better grain-interconnectivity.

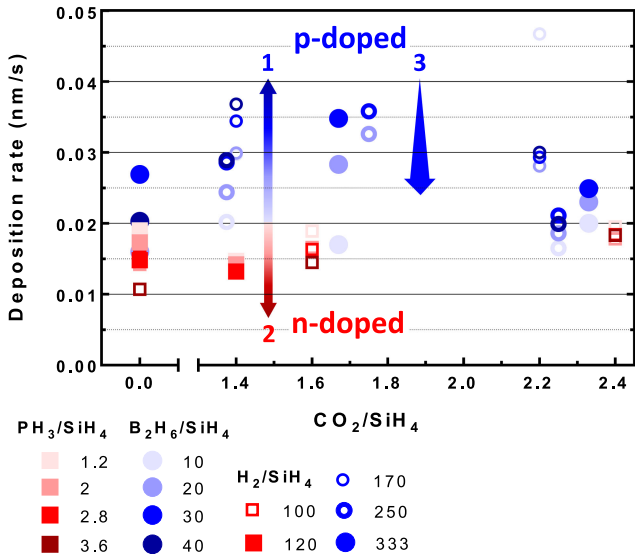

Fig. 5. Deposition rate of n-doped (red, squares) and p-doped (blue, circles) a/nc-$SiO_{X\geq 0}$:H films, as a function of $F_{CO2/SiH4}$. The brightness/depth of color of the markers indicates the $F_{PH3/SiH4}$ while the size of the markers and their open/closed nature indicates the $F_{H2/SiH4}$. Arrows, added to indicate trends in the data, are referenced in the article. ↑1-2 indicate the influence of $F_{B2H6/SiH4}$ and $F_{PH3/SiH4}$. ↑3 indicates the influence of $F_{H2/SiH4}$.

This is in line with reports from [27] and [28]. The influence of $F_{H2/SiH4}$ on E_{04} is not conclusive from the presented results.

$F_{B2H6/SiH4}$ significantly affects the material growth. For the electrical properties, two different trends are visible. Increasing the doping flow rate significantly increases the E_{act} of the films (see Fig. 3 ↑4). The E_{act} increases from 110 to 443 meV at $F_{CO2/SiH4} = 1.4$ and from 173 to 470 meV at $F_{CO2/SiH4} = 2.2$ when $F_{B2H6/SiH4}$ is increased from 10 to 40. However, in the deposition regime where a relatively high CO_2 and H_2 flow rate are used (see Fig. 3 ↑5), a higher $F_{B2H6/SiH4}$ actually leads to a decrease of the E_{act}. We believe that the doping flow rate has two competing effects. For one, the dopant precursor suppresses crystalline growth. If, on the other hand, the films are relatively crystalline, an increase of $F_{B2H6/SiH4}$ can lead to a more conductive film through a larger active dopant concentration.

Understanding this requires some insight into the integration and ionization behavior of boron in a mixed phase material. For one, the doping efficiency in the amorphous phase is very low, since no substitutional doping occurs in a material lacking long range order [29], [30]. Instead, a small fraction of dopants in an amorphous network result in ionized defects, as a consequence of induced structural disorder [31], [32]. In the crystalline phase, a boron atom is much more likely to be active, as it substitutes a silicon atom in the lattice. It has been reported however that boron preferentially resides at the boundary of crystalline grains in an amorphous matrix, where it is predominantly inactive [33], [34]. At higher crystalline fractions, both the ratio of the crystalline to amorphous phase as well as the crystalline grain bulk versus grain surface ratio is increased. We speculate that this larger fraction of crystalline silicon sites, with respect to c-Si grain boundaries and amorphous sites, makes it more likely that boron integrated in the mixed phase growth results in an active dopant. For most films an increase of $F_{B2H6/SiH4}$ suppresses crystalline growth, thereby deteriorating the macroscopic conductive properties of the films and hardly increasing the active dopant concentration in the largely amorphous films. A decreased E_{act} with an increased $F_{B2H6/SiH4}$ is, therefore, only observed for the films with a high $F_{H2/SiH4}$. For these films the nucleation suppressive behavior of the dopant gas is compensated by the nucleation promoting behavior of the hydrogen. The macroscopic conductive properties are hardly affected and the active dopant concentration in these relatively crystalline films is increased.

Finally, an increase of $F_{B2H6/SiH4}$ decreases the E_{04} (see Fig. 3 ↑6), regardless of the other precursor gasses. Increasing $F_{B2H6/SiH4}$ from 10 to 40, for example, decreases the E_{04} from 2.03 to 1.95 eV at $F_{CO2/SiH4}\approx 1.8$ and from 2.25 to 2.10 eV at $F_{CO2/SiH4}\approx 2.3$. This is most likely a result of the decreased oxygenation of the material with increasing $F_{B2H6/SiH4}$. However, a decrease of E_{04} as a result of a decreasing hydrogen concentration with increasing $F_{B2H6/SiH4}$, as observed in p-doped amorphous silicon in [35] and [36], cannot be excluded.

The n-doped films generally show the same trends, although higher optical bandgaps and lower activation energies are achieved. For the samples with a relatively high $F_{H2/SiH4}$ the E_{act} increases significantly by about 40–60 meV when CO_2 is introduced during deposition (see Fig. 4 ↑1). The E_{act} of the films deposited at lower $F_{H2/SiH4}$ ratio are not significantly influenced by the $F_{CO2/SiH4}$. The E_{04} increases with increasing $F_{CO2/SiH4}$ (see Fig. 4 ↑2) as expected. As with the p-doped films, an increase of the relative doping flow rate decreases the E_{04} of the films (see Fig. 4 ↑3). An increase of $F_{H2/SiH4}$, finally, significantly decreases the E_{act} of the nc-Si:H films (see Fig. 4 ↑4), within a certain range. It should be noted that at a relative flow rate of $F_{H2/SiH4} = 140$ the films became highly transparent with activation energies of 500 meV and higher.

The precursor gas flow rates also influence the deposition rate of the doped films. An increase of the diborane gas flow rate, for instance, strongly increases the deposition rate (see Fig. 5 ↑1), which is in line with earlier reports [16], [37], [38]. Diborane easily dissociates. Created radicals could have two possible effects resulting in the deposition rate increase. Enhance the dissociation of silane in the plasma, thereby increasing the flux of SiH_X radicals to the surface. Increase the dangling bond density at the surface, thereby increasing the amount of growth sites for silicon radicals. It has been proposed that the increased dangling bond density at the surface is a result of the ability of Hydroboron BH_3 radicals, that are readily formed in the plasma from the B_2H_6 precursor, to strip the surface of hydrogen through the formation of metastable BH_5 reactive intermediates [39], [40]. This increases the SiH_3 adsorption rate and therefore the silicon growth flux. An increase of the relative phosphine flow has the opposite effect (see Fig. 5 ↑2). The mechanism behind this is unclear.

An increase of the relative H_2 flow rate decreases the growth rate (see Fig. 5 ↑3). This is most likely a result of atomic hydrogen induced etching, which is enhanced with respect to the silicon growth flux under higher hydrogen dilution conditions. Indeed it has been reported for p-type a-Si:H films the void fraction decreases with increasing $F_{H2/SiH4}$ [37]. Moreover, since the low growth rate conditions are accompanied by a

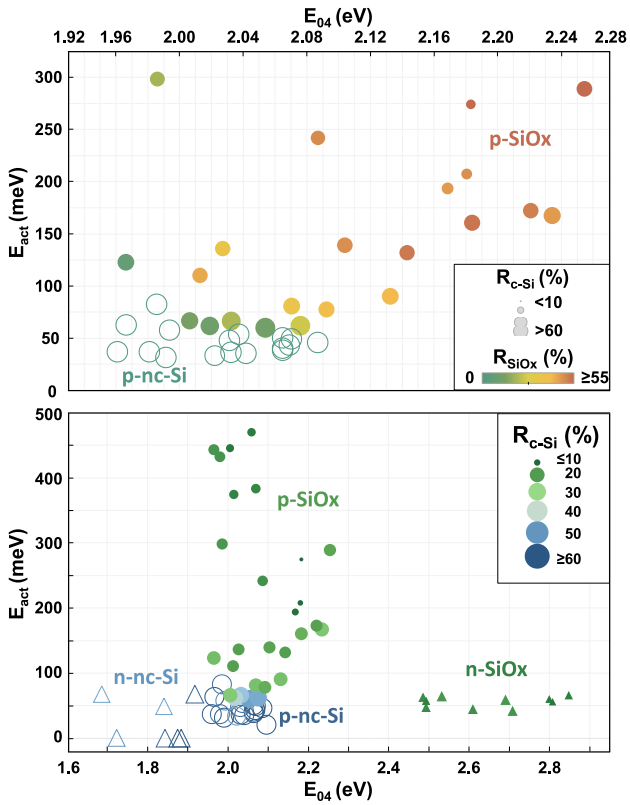

Fig. 6. E_{act} as a function of E_{04} for all doped a/nc-$SiO_{X\geq 0}$:H samples (bottom) and exclusively p-type a/nc-$SiO_{X\geq 0}$:H samples (top). nc-Si:H samples are represented by open symbols, while SiO_X:H samples are represented by closed symbols. P-doped samples are represented by circles, while n-doped symbols (bottom plot) are represented by triangles. In the top plot, the color and brightness of the symbols indicates R_{SiOx}, while the size of the symbols indicates $R_{c\text{-}Si}$. In the bottom plot both symbol color/brightness and size indicate $R_{c\text{-}Si}$.

larger atomic hydrogen flux to the substrate, the crystallization of the silicon phase is enhanced. This explains the nucleation promoting behavior of an increased relative H_2 flow rate.

Manipulation of doped silicon material growth is achieved through the relative gas flow rates. Naturally, the extent of manipulation is limited. In Fig. 6 (bottom), the tradeoff between the E_{act} and E_{04} of all doped films is shown. A few things are apparent from this Fig.. 1. The lowest activation energies are achieved for the doped nc-Si:H samples. For $R_{SiOx}>0$ both E_{act} and E_{04} increase. This is directly related to $R_{c\text{-}Si}$, which is indicated in Fig. 6(bottom) through icon size and color. Although they have similar $F_{CO2/SiH4}$, the E_{04} of n-doped samples is higher than that of their p-doped counterparts. This is a result of higher R_{SiOx} with respect to the p-doped samples. The mechanism behind this is unclear. 3. Despite the high R_{SiOx} and $E_{04}$of the n-doped SiO_X:H samples, they retain relatively low E_{act}. This is unlike the p-doped samples where small changes have a strong effect on the optoelectrical performance. We can therefore reflect that the nature of the a/nc-$SiO_{X\geq 0}$:H material is such that it favours n-type doping. This could be result of the fact that undoped amorphous silicon tissue by itself is slightly n-type and becomes more n-type when oxygen is introduced [41], [42]. Alternatively, it could be the result of the deposition-rate-decreasing effect of

TABLE II
PRECURSOR GAS FLOW RATES OF FILMS USED IN FIG 7

	p-SiOx:H	p-SiOx:H 2	p-nc-Si:H	p-nc-Si:H 2
SiH_4 (sccm)	0.8	0.8	0.8	0.6
B_2H_6 (sccm)	10	20	20	32
H_2 (sccm)	170	170	170	200
CO_2 (sccm)	2.3	2		

phosphine with respect to diborane, as shown in Fig. 5, resulting in a denser, less defective material. Or perhaps that phosphine favourably resides inside crystalline grains, as reported in [33], as opposed to near the grain boundaries or in the amorphous phase, resulting in a higher doping efficiency. Regardless of the reason, the results show that optimization of the p-doped layer, often crucial for device performance due to its placement between the absorber layer and incident light, is challenging. For this reason, Fig. 6(top) shows the p-doped samples in particular, with the additional information of the R_{SiOx}.

From Fig. 6(top) it is again clear that increased oxygenation inevitably leads to higher activation energies. The lowest E_{act} are achieved by the p-nc-Si:H samples, which also have the lowest E_{04}, ranging from ∼1.96-2.06 eV. This range of optical bandgap energies is likely because in the spectral range where the E_{04} is determined, the absorption is dominated by the amorphous phase in the doped a/nc-$SiO_{X\geq 0}$:H material. The E_{04} therefore provides information on the quality of the amorphous tissue between the nanocrystalline phase. The band gap of this amorphous tissue is determined by two factors. First, the optical bandgap energy will increase with increased porosity of amorphous phase. Second, the optical gap will increase with increased oxygenation. This is demonstrated in Fig. 6, since E_{04} is only increased above ∼2.1eV when the amorphous phase becomes increasingly oxygenated.

B. Investigation of Thickness

We have described the complex interplay between crystalline growth, oxygenation, and dopant integration in the doped a/nc-$SiO_{X\geq 0}$:H films. The material properties of the doped films, when integrated in devices, does not exclusively depend on the deposition conditions, however. The optoelectrical properties of the doped layers are not uniform in the growth direction.

Fig.7 (left) shows the E_{act} and E_{04} of p-nc-Si:H and p-SiO_X:H films deposited at different thicknesses and two sets of deposition conditions. The deposition conditions are given in Table II It can be observed that the E_{act} decreases with increasing film thickness for both the oxygenated and oxygen-free doped silicon films. This is directly related to the crystallinity. The Raman shift of the p-doped films is plotted in Fig. 7 (right). There are four amorphous silicon peaks indicated, corresponding to the TA mode at 160 cm^{-1}, the LA mode at 320 cm^{-1}, the LO mode at 390 cm^{-1} and the TO mode at 320 cm^{-1}. It can be seen that with increasing thickness, the intensity of the Raman shift peak at 520 cm^{-1}, which corresponds to the crystalline silicon phase, increases with respect to the amorphous silicon peaks. This observation, the increased crystallinity in the growth

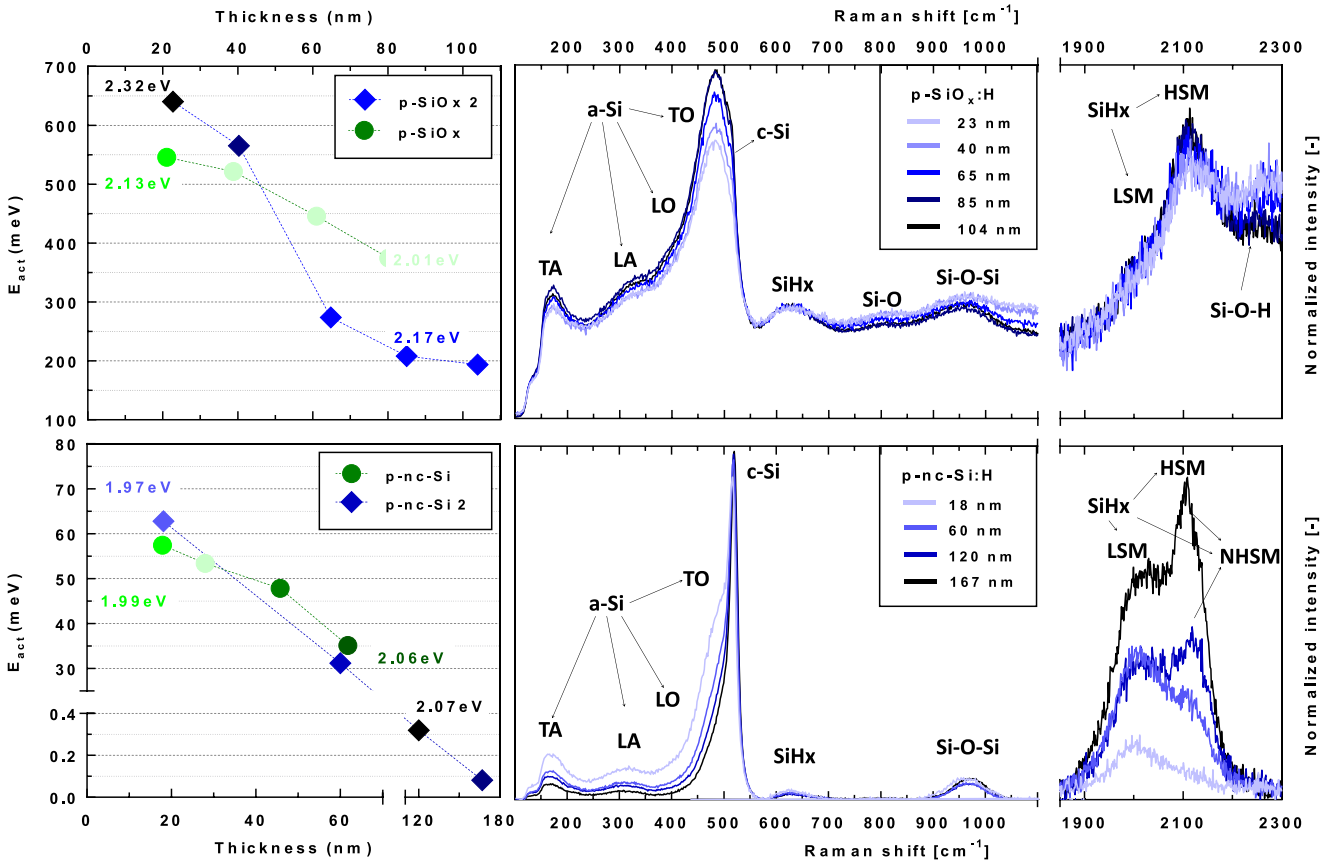

Fig. 7. Material properties as a function of thickness. The plot on the left shows E_{act} as a function of thickness for two sets of p-SiO$_X$:H films (left, top) and two sets of p-nc-Si:H films (left, bottom). The brightness of color of the icons indicates the E_{04} from lowest (bright) to highest (dark) value within the series. The lowest and highest E_{04} values are indicated in article in the plots. Structural analysis of these samples is shown in the plots on the right. These plots show the normalized count rate as a function of Raman shift for the p-SiO$_X$ 2 samples (right, top) and the p-nc-Si 2 samples (right, bottom) processed at different thicknesses, as indicated in the legend. Suspected identification of the observed peaks is indicated in the graphs. For the p-nc-Si:H samples the background was subtracted manually.

direction, is in line with earlier reports, where development of crystalline filaments in the growth direction was demonstrated [11], [13], [43], [44].

The thickness of the films also influences the optical bandgap energy. For the p-SiO$_x$:H films the E_{04} decreases with increasing thickness. This is likely the results of a decreased silicon-oxide phase fraction. The R_{SiOx} obtained from SE measurements decreased from 64% to at 23 nm to 47% at 104 nm. This decrease of the R_{SiOx} can also be observed in Fig. 7 (top, right), by a decrease of the silicon-oxygen bond related Raman shift peaks. These peaks are the Raman shift peak at 795 cm^{-1} related to Si-O stretching [45], the broad peak at roughly 900–1100 cm^{-1} related to Si-O-Si stretching modes [46], [47] and the peak at 2250 cm^{-1}, related to the Si-O-H stretching modes [46], [48]. All these SiO$_X$ related Raman peak intensities decrease with increasing thickness, while the amorphous silicon peaks increase. It should be noted that some influence of the glass substrates on the Raman spectra cannot be excluded. This said, the trends are confirmed with SE measurements where the influence of the substrate is excluded.

The E_{04} of the p-nc-Si:H samples on the other hand increases with increasing thickness. This is likely the result of the amorphous phase growing more porous along the growth direction. More precisely, the density of the amorphous phase is related to the organization of the silicon-hydrides in the amorphous network. When distributed monohydrides are increasingly organized in multivacancies and small voids, the density of the network decreases and the optical bandgap increases [49], [50]. This can be corroborated by a distinct signature in the Raman spectrum in the 1800–2200 cm^{-1} range. This range, related to the silicon-hydride stretching modes, can be simplified into a low stretching mode (LSM) peak at roughly 2000 cm^{-1} and a high stretching mode peak (HSM) at roughly 2100 cm^{-1} [46]. The LSM corresponds to mono configurations, while the HSM corresponds to silicon-hydrides and di-hydrides organized in small vacancies and voids [15], [51]. In addition in the 2100–2103 cm^{-1} range a narrow signature of the extreme high stretching modes (NHSMs) [46].These stretching modes reflect the mono- and di-hydrides on the surface of crystalline silicon grains. Fig. 7 (bottom, right) shows that with increasing p-nc-Si:H thickness the NHSM peak strongly increases with respect to the LSM peak, indicating an increase of hydrogenated c-Si grain boundaries not passivated by a-Si:H tissue. Subsequently the amorphous tissue between the grains becomes more

porous. This increased porosity of the amorphous phase along the growth direction is similar to the development of a-Si bulk properties in the growth direction [52].

IV. Summary

In this article, we have investigated how the optoelectrical properties of doped silicon films are determined by the different phases, and their relative fractions, present in the doped heterogeneous a/nc-$SiO_{X\geq 0}$:H material. Using a material phase diagram, we have visualized how the relative nanocrystalline silicon, amorphous silicon and amorphous silicon-oxide fractions can be manipulated through changes in the precursor gas flow rates. Moreover, we discussed how these material phases, in combination with the density of the a-$SiO_{X\geq 0}$:H phase and the extent of doping, influence the optoelectrical properties of the processed films.

An increase of the relative CO_2 flow rate leads to increased oxygenation of the amorphous phase, which predominantly results in a higher optical bandgap. An increase of doping gas flow rate suppresses crystalline growth, decreases the oxygen content and, if the material is sufficiently crystalline, increases the active doping concentration. Sufficient crystallinity can be achieved by increasing the relative hydrogen flow rate, which decreases the deposition rate, resulting in denser and more crystalline material growth. However, if the relative hydrogen flow rate exceeds a certain threshold, the balance between the silicon growth flux an atomic hydrogen etching is upset, resulting in poor electrical properties with activation energies of 500 meV and up.

We also demonstrate that the optoelectrical properties are not uniform along the growth direction. For p-doped a/nc-$SiO_{X\geq 0}$:H films the activation energy decreases with increasing film thickness, as a function of the crystalline fraction. The optical bandgap energy of p-SiO_X:H films decreases with thickness, as a result of a decreased amorphous silicon oxide material phase fraction. The optical bandgap energy of the p-nc-Si:H films increases with thickness due to increased porosity of the amorphous phase along the growth direction.

References

[1] M. Izzi *et al.*, "Doped SiO x emitter layer in amorphous/crystalline silicon heterojunction solar cell," *Appl. Phys. A*, vol. 115, no. 2, pp. 705–712, May 2014.

[2] K. Ding, U. Aeberhard, F. Finger, and U. Rau, "Silicon heterojunction solar cell with amorphous silicon oxide buffer and microcrystalline silicon oxide contact layers," *Physica Status Solidi, Rapid Res. Lett.*, vol. 195, no. 6, pp. 193–195, 2012.

[3] S. Rattanapan, T. Watahiki, S. Miyajima, and M. Konagai, "Improvement of rear surface passivation quality in p-Type silicon heterojunction solar cells using boron-doped microcrystalline silicon oxide," *Jpn. J. Appl. Phys.*, vol. 50, no. 8, Aug. 2011, Art. no. 082301.

[4] A. J. Blanker *et al.*, "Advanced light management techniques for two-terminal hybrid tandem solar cells," *Sol. Energy Mater. Sol. Cells*, vol. 181, pp. 77–82, Jul. 2018.

[5] P. Buehlmann *et al.*, "In situ silicon oxide based intermediate reflector for thin-film silicon micromorph solar cells," *Appl. Phys. Lett.*, vol. 91, no. 14, Oct. 2007, Art. no. 143505.

[6] L. V. Mercaldo, P. Delli Veneri, I. Usatii, E. M. Esposito, and G. Nicotra, "Properties of mixed phase n-doped silicon oxide layers and application in micromorph solar cells," *Sol. Energy Mater. Sol. Cells*, vol. 119, pp. 67–72, Dec. 2013.

[7] J. S. Cashmore *et al.*, "Improved conversion efficiencies of thin-film silicon tandem (MICROMORPH^{TM}) photovoltaic modules," *Sol. Energy Mater. Sol. Cells*, vol. 144, pp. 84–95, Jan. 2016.

[8] F. Hou *et al.*, "Inverted pyramidally-textured PDMS antireflective foils for perovskite/silicon tandem solar cells with flat top cell," *Nano Energy*, vol. 56, Oct. 2018, pp. 234–240, 2019.

[9] M. Boccard *et al.*, "Substrate dependent stability and interplay between optical and electrical properties in μc-Si:H single junction solar cells," *Sol. Energy Mater. Sol. Cells*, vol. 95, no. 1, pp. 195–198, Jan. 2011.

[10] V. Smirnov, A. Lambertz, B. Grootoonk, R. Carius, and F. Finger, "Microcrystalline silicon oxide (μc-SiOx:H) alloys: A versatile material for application in thin film silicon single and tandem junction solar cells," *J. Non-Cryst. Solids*, vol. 358, no. 17, pp. 1954–1957, Sep. 2012.

[11] P. Babal *et al.*, "Nanostructure analysis of P-Doped nanocrystalline silicon oxide," in *Proc. 28th Eur. Photovolt. Sol. Energy Conf. Exhib*. 2020, pp. 2580–2587.

[12] A. Richter, L. Zhao, F. Finger, and K. Ding, "Nano-composite microstructure model for the classification of hydrogenated nanocrystalline silicon oxide thin films," *Surf. Coatings Technol.*, vol. 295, pp. 119–124, Jun. 2016.

[13] V. Smirnov *et al.*, "Doped microcrystalline silicon oxide alloys for silicon-based photovoltaics: Optoelectronic properties, chemical composition, and structure studied by advanced characterization techniques," *Phys. Status Solidi*, vol. 213, no. 7, pp. 1814–1820, Jul. 2016.

[14] T. de Vrijer, F. T. Si, H. Tan, and A. H. M. Smets, "Chemical stability and performance of doped silicon oxide layers for use in thin film silicon solar cells," *IEEE J. Photovolt.*, vol. 9, no. 1, pp. 3–11, Jun. 2019.

[15] A. H. M. Smets *et al.*, "The relation between the bandgap and the anisotropic nature of hydrogenated amorphous silicon," *IEEE J. Photovolt.*, vol. 2, no. 2, pp. 94–98, Apr. 2012.

[16] P. Babál, "Doped nanocrystalline silicon oxide for use as (intermediate) reflecting layers in thin film silicon solar cells," 2014.

[17] C. M. Herzinger, B. Johs, W. A. McGahan, J. A. Woollam, and W. Paulson, "Ellipsometric determination of optical constants for silicon and thermally grown silicon dioxide via a multi-sample, multi-wavelength, multi-angle investigation," *J. Appl. Phys.*, vol. 83, no. 6, pp. 3323–3336, Mar. 1998.

[18] H. Tan, P. Babal, M. Zeman, and A. H. M. Smets, "Solar energy materials & solar cells wide bandgap p-type nanocrystalline silicon oxide as window layer for high performance thin- film silicon multi-junction solar cells," *Sol. Energy Mater. Sol. Cells*, vol. 132, pp. 597–605, 2015.

[19] P. Delli Veneri, L. V. Mercaldo, and I. Usatii, "Silicon oxide based n-doped layer for improved performance of thin film silicon solar cells," *Appl. Phys. Lett.*, vol. 97, no. 2, Jul. 2010, Art. no. 023512.

[20] R. Biron, C. Pahud, F. Haug, and C. Ballif, "Origin of the voc enhancement with a p-doped nc-SiOx:H window layer in nip solar cells," *J. Non-Cryst. Solids*, vol. 358, no. 17, pp. 1958–1961, Sep. 2012.

[21] D. M. Zhigunov, G. N. Kamaev, P. K. Kashkarov, and V. A. Volodin, "On raman scattering cross section ratio of crystalline and microcrystalline to amorphous silicon," *Appl. Phys. Lett.*, vol. 113, no. 2, Jul. 2018, Art. no. 023101.

[22] C. Smit *et al.*, "Determining the material structure of microcrystalline silicon from Raman spectra," *J. Appl. Phys.*, vol. 94, no. 5, pp. 3582–3588, Sep. 2003.

[23] P. Cuony *et al.*, "Mixed-phase p-type silicon oxide containing silicon nanocrystals and its role in thin-film silicon solar cells," *Appl. Phys. Lett.*, vol. 97, no. 21, Nov. 2010, Art. no. 213502.

[24] C. Song, X. Wang, R. Huang, J. Song, and Y. Guo, "Effects of doping concentration on the microstructural and optoelectrical properties of boron doped amorphous and nanocrystalline silicon films," *Mater. Chem. Phys.*, vol. 142, no. 1, pp. 292–296, Oct. 2013.

[25] D. Y. Kim, E. Guijt, R. A. C. M. M. van Swaaij, and M. Zeman, "Development of a-SiOx:H solar cells with very high Voc×FF product," *Prog. Photovolt. Res. Appl.*, vol. 23, pp. 671–684, 2015.

[26] S. Kirner, O. Gabriel, B. Stannowski, B. Rech, and R. Schlatmann, "The growth of microcrystalline silicon oxide thin films studied by in situ plasma diagnostics," *Appl. Phys. Lett.*, vol. 102, no. 5, Feb. 2013, Art. no. 051906.

[27] O. Gabriel *et al.*, "On the plasma chemistry during plasma enhanced chemical vapor deposition of microcrystalline silicon oxides," *Plasma Process. Polym.*, vol. 12, no. 1, pp. 82–91, Jan. 2015.

[28] A. Lambertz, T. Grundler, and F. Finger, "Hydrogenated amorphous silicon oxide containing a microcrystalline silicon phase and usage as an intermediate reflector in thin-film silicon solar cells," *J. Appl. Phys.*, vol. 109, no. 11, Jun. 2011, Art. no. 113109.

[29] S. G. Bishop and S. E. Carlos, "Studies of hydrogenated amorphous silicon," 1984.
[30] M. de Lima and F. Marques, "On the doping mechanism of boron-doped hydrogenated amorphous silicon deposited by rf-co-sputtering," *J. Non-Cryst. Solids*, vol. 299–302, pp. 605–609, Apr. 2002.
[31] D. Caputo, G. de Cesare, F. Irrera, A. Nascetti, and F. Palma, "On the relation between defect density and dopant concentration in amorphous silicon films," *J. Non-Cryst. Solids*, vol. 266–269, pp. 565–568, May 2000.
[32] W. B. Jackson and N. M. Amer, "Direct measurement of gap-state absorption in hydrogenated amorphous silicon by photothermal deflection spectroscopy," *Phys. Rev. B*, vol. 25, no. 8, pp. 5559–5562, Apr. 1982.
[33] R. Guerra and S. Ossicini, "Preferential positioning of dopants and co-dopants in embedded and freestanding Si nanocrystals," *J. Amer. Chem. Soc.*, vol. 136, no. 11, pp. 4404–4409, Mar. 2014.
[34] S. H. Hong *et al.*, "Active doping of B in silicon nanostructures and development of a Si quantum dot solar cell," *Nanotechnology*, vol. 22, no. 42, Oct. 2011, Art. no. 425203.
[35] J. M. Westra, "Solid phase crystallisation of hydrogenated amorphous silicon deposited by ETPCVD on glass," 2018.
[36] S. Ray, P. Chaudhuri, A. K. Batabyal, and A. K. Barua, "Electronic and optical properties of boron doped hydrogenated amorphous silicon thin films," *Sol. Energy Mater.*, vol. 10, pp. 335–347, 1984.
[37] D. B. Saint John *et al.*, "Influence of microstructure and composition on hydrogenated silicon thin film properties for uncooled microbolometer applications," *J. Appl. Phys.*, vol. 110, no. 3, Aug. 2011, Art. no. 033714.
[38] H. Fujiwara and M. Kondo, "Real-time monitoring and process control in amorphous/crystalline silicon heterojunction solar cells by spectroscopic ellipsometry and infrared spectroscopy," *Appl. Phys. Lett.*, vol. 86, no. 3, Jan. 2005, Art. no. 032112.
[39] J. Perrin, Y. Takeda, N. Hirano, Y. Takeuchi, and A. Matsuda, "Sticking and recombination of the SiH_3, radical on hydrogenated amorphous silicon: The catalytic effect of diborane," *Surf. Sci.*, vol. 210, pp. 114–128, 1989.
[40] I. M. Pepperberg, T. A. Halgren, and W. N. Lipscomb, "Extended topological rules for boron hydrides. 1. Structures and relative energies for the transient boron hydrides diborane(4), triborane(7), triborane(9), tetraborane(8), and tetraborane(12)," *Inorg. Chem.*, vol. 16, no. 2, pp. 363–379, Feb. 1977.
[41] A. Morimoto, M. Matsumoto, M. Yoshita, M. Kumeda, and T. Shimizu, "Doping effect of oxygen or nitrogen impurity in hydrogenated amorphous silicon films," *Appl. Phys. Lett.*, vol. 59, no. 17, pp. 2130–2132, Oct. 1991.
[42] K. Jiranapakul, K. Shirakawa, and J. Shirafuji, "Photoelectric properties of oxygen-doped a-Si:H prepared by rf sputtering," *Jpn. J. Appl. Phys.*, vol. 25, no. 10, pp. 1457–1464, Oct. 1986.
[43] P. Cuony *et al.*, "Silicon filaments in silicon oxide for next-generation photovoltaics," *Adv. Mater.*, vol. 24, no. 9, pp. 1182–1186, Mar. 2012.
[44] M. Klingsporn *et al.*, "Resolving the nanostructure of plasma-enhanced chemical vapor deposited nanocrystalline SiO $\times$ layers for application in solar cells," *J. Appl. Phys.*, vol. 119, no. 22, Jun. 2016, Art. no. 223104.
[45] Z. P. Wang, H. X. Han, X. S. Zhao, and G. H. Li, "Si-Cl bonds in A-Si: H: Cl films," *Solid State Commun.,* vol. 58, no. 10, pp. 709–711, 1986.
[46] A. H. M. Smets, T. Matsui, and M. Kondo, "High-rate deposition of microcrystalline silicon pin solar cells in the high pressure depletion regime," *J. Appl. Phys.*, vol. 104, no. 3, Aug. 2008, Art. no. 034508.
[47] A. C. Bronneberg, A. H. M. Smets, M. Creatore, and M. C. M. van de Sanden, "On the oxidation mechanism of microcrystalline silicon thin films studied by fourier transform infrared spectroscopy," *J. Non-Cryst. Solids*, vol. 357, no. 3, pp. 884–887, Feb. 2011.
[48] K. Kawamura, S. Ishizuka, H. Sakaue, and Y. Horiike, "Diagnostics of hydrogen role in the Si surface reaction processes employing In-situ fourier transform infrared-attenuated total reflection," *Jpn. J. Appl. Phys.*, vol. 30, pp. 3215–3218, Nov. 1991.
[49] M. Mews, T. F. Schulze, N. Mingirulli, and L. Korte, "Hydrogen plasma treatments for passivation of amorphous-crystalline silicon-heterojunctions on surfaces promoting epitaxy," *Appl. Phys. Lett.*, vol. 102, no. 12, Mar. 2013, Art. no. 122106.
[50] M. Fischer *et al.*, "High pressure processing of hydrogenated amorphous silicon solar cells: Relation between nanostructure and high open-circuit voltage," *Appl. Phys. Lett.*, vol. 106, no. 4, Jan. 2015, Art. no. 043905.
[51] A. H. M. Smets and M. C. M. van de Sanden, "Relation of the Si-H stretching frequency to the nanostructural Si-H bulk environment," *Phys. Rev. B*, vol. 76, no. 7, Aug. 2007, Art. no. 073202.
[52] M. A. Wank, R. A. C. M. M. van Swaaij, P. Kudlacek, M. C. M. van de Sanden, and M. Zeman, "Hydrogenated amorphous silicon deposited under accurately controlled ion bombardment using pulse-shaped substrate biasing," *J. Appl. Phys.*, vol. 108, no. 10, Nov. 2010, Art. no. 103304.